

Multi-Grid Back-Projection Networks

Pablo Navarrete Michelini, *Member, IEEE*, Wenbin Chen, Hanwen Liu, Dan Zhu, Xingqun Jiang

Abstract—Multi-Grid Back-Projection (MGBP) is a fully-convolutional network architecture that can learn to restore images and videos with upscaling artifacts. Using the same strategy of multi-grid partial differential equation (PDE) solvers this multiscale architecture scales computational complexity efficiently with increasing output resolutions. The basic processing block is inspired in the iterative back-projection (IBP) algorithm and constitutes a type of cross-scale residual block with feedback from low resolution references. The architecture performs in par with state-of-the-arts alternatives for regression targets that aim to recover an exact copy of a high resolution image or video from which only a downscale image is known. A perceptual quality target aims to create more realistic outputs by introducing artificial changes that can be different from a high resolution original content as long as they are consistent with the low resolution input. For this target we propose a strategy using noise inputs in different resolution scales to control the amount of artificial details generated in the output. The noise input controls the amount of innovation that the network uses to create artificial realistic details. The effectiveness of this strategy is shown in benchmarks and it is explained as a particular strategy to traverse the perception-distortion plane.

Index Terms—multigrid, iterative backprojection, super resolution, convolutional networks.

I. INTRODUCTION

IMAGE and video upscaling has been studied for decades and remains an active topic of research because of constant technological advances in digital imaging. One scenario where upscaling is now more demanding arises in digital display technologies, where new standards like BT.2020 [1] are introduced. The resolution of digital displays has experienced a tremendous growth over the past few decades, as shown in Figure 1. The transition between different formats leads to a challenging problem. On one hand, large amount of digital content still exist in popular old standards such as standard-definition (SD). On the other hand, the latest display technologies (e.g. 4K, 8K and above) are expected to show this content with reasonable quality. Standard upscaling technologies are clearly insufficient for this purpose. While a $2\times$ upscaler maps 1 input pixel into 4 output pixels, an $8\times$ upscaler maps 1 input pixel into 64 output pixels, which already can contain a small image. The problem demands advanced solutions that are capable of understanding the content and filling in these large pieces of images with visually appealing and consistent information. In particular, large upscaling factors are needed to convert SD to ultra high-definition (UHD) resolutions. Thus, large upscaling represents a real problem in current market and

it is expected to persist and become even more challenging with the rapid development of new technologies.

In classical interpolation theory, upscaling images by integer factors is explained as two sequential processes: upsample (insert zeros) and filter [2], [3]. Standard upscaler algorithms, such as Bicubic or Lanczos, find high-resolution images with a narrow frequency content by using fixed low-pass filters. Modern tensor processing frameworks (e.g. Pytorch, Tensorflow, etc.) implement this process using a so-called *strided transposed convolutional layer*. Similarly, the image acquisition process can be modeled as: filter and downsample (drop samples). Many times we know the explicit model, e.g. bicubic downscaler. Tensor processing frameworks implement this process using a *strided convolutional layer*.

More advanced upscalers have followed geometric principles to improve image quality. For example, *edge-directed interpolation* uses adaptive filters to improve edge smoothness [4], [5], or *bandlet* methods use both adaptive upsampling and filtering [6]. Later on, machine learning has been able to use examples of pristine high-resolution images to learn a mapping from low-resolution [7]. The rise of deep-learning and convolutional networks in image classification tasks [8] quickly saw a series of important improvements in image resizing with large upscaling factors, which is the process widely known as image super-resolution (SR). Major progress in network architectures for image classification often succeeded in image SR, as seen for example with CNNs applied in SR-CNN [9], ResNets [10] applied in EDSR [11], DenseNets [12] applied in RDN [13], attention [14] applied in RCAN [15], and non-local attention [16] applied in RNAN [17]. In all these examples, arguably the most influential practice is the use of residual networks (ResNets).

For video content, single frame upscaling would loose the

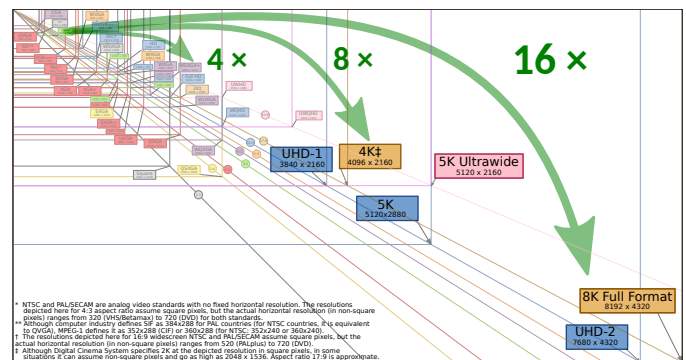


Fig. 1. The dramatic growth of standard resolutions demands the development of Super-Resolution technologies to resize image with large upscaling factors. Source: [Wikimedia CC BY-SA](#).

Pablo Navarrete M., Wenbin Chen, Hanwen Liu, Dan Zhu, and Xingqun Jiang are with the Department of Artificial Intelligence, BOE Technology Group Co., Ltd., Beijing, China.

Manuscript received July 1st, 2020. First revision November 17th, 2020. Second revision December 23rd, 2020. Accepted December 28th, 2020.

chance of improving quality by learning temporal correlations and can result in visible flickering artifacts at large upscaling factors. Popular approaches to capture temporal information include: methods that align neighbor frames in addition to solve single image artifacts [18]–[20], network architectures that use motion compensation to align neighbor frames [21]–[24], use transformer blocks to learn the optical flow [25], learn dynamic upscaling filters [26], and more recently use deformable convolutions for frame alignment [27]. To better understand the mechanisms used to extend image to video SR we describe some of these solution in more detail:

- TOFlow [25] is a network designed with motion estimation and video processing components. It combines three modules to: 1) estimate the motion fields between input frames; 2) register all input frames based on estimated motion fields; and 3) generate target output from registered frames. These three modules are jointly trained to minimize the loss between output frames and ground truth.
- Dynamic Upsampling Filters (DUF) [26] is a network that generates dynamic upsampling filters and a residual image, which are computed depending on the local spatio-temporal neighborhood of each pixel to avoid explicit motion compensation. A HR image is reconstructed directly from the input image using the dynamic upsampling filters, and the fine details are added through the computed residual.
- Enhanced Deformable convolutions Video Restoration (EDVR) [27] is a network that combines frame alignment and spatio-temporal fusion. To handle large motions it uses a Pyramid, Cascading and Deformable (PCD) alignment module, in which frame alignment is done at the feature level using deformable convolutions in a coarse-to-fine manner. Then they use a Temporal and Spatial Attention (TSA) fusion module, in which attention is applied both temporally and spatially to emphasize important features for subsequent restoration.
- The Video Enhancement and Super-Resolution network (VESR-Net) [28] uses both PCD alignment and a Separate Non-Local attention (SNL) module to aggregate the information among different frames. For reconstruction, they utilize stacked channel-attention residual block (CARB) [29] followed by a feature decoder. Finally, Efficient Video Enhancement and Super-Resolution Net (EVESR-Net) [30] improved VESR-Net replacing the SNL module with an Efficient Point-Wise Temporal Attention Block (EPAB) that aggregates the spatio-temporal information with less operations and memory consumption.

The optimization problem of learning to map images/videos from low to high resolution can have two distinctive targets:

- **High Fidelity**, the aim is to obtain a solution capable to produce high resolution results with the best fidelity (PSNR) to the ground truth. This is also known as a *low distortion* target where *distortion* refers to a measure of the difference between output content and ground truth.
- **Perceptual Quality**, the aim is to obtain a solution capable to produce high resolution results with the best perceptual quality similar to the ground truth.

Historically, high fidelity was the major focus of research

in image SR until systems became more efficient and large upscaling factors were considered. The empirical evidence then showed that high fidelity often leads to cartoonish effects that are easily recognizable and looked far from real photographs. Soon this reveal a fundamental phenomena that is now known as the *Perception-Distortion* trade-off established by Blau and Michaeli in [31]. That is, both perception and distortion targets cannot be achieved at the same time, one must compromise perceptual quality to improve fidelity and vice versa. The trade-off also motivated the first workshop and challenge focused on perceptual super-resolution (PIRM 2018 [32]) that strongly confirmed and gave further insight into this principle.

Here, we present our contributions to the development of new image and video super-resolution technologies with major focus on: deep-learning architectures, and training strategies for perceptual super-resolution. First, we propose a deep learning architecture called Multi-Grid Back-Projection (MGBP) [33]–[35] that has the following important characteristics:

- It uses a *back-projection* residual strategy that moves features from high to low resolution to compare them with a low resolution reference and then comes back to correct the high resolution feature. This is analogous to the iterative back-projection (IBP) algorithm but its target is more far reaching as a general learning module that aims to improve the high resolution output in successive iterations.
- It uses a *multi-grid* recursive strategy using back-projection residual blocks within back-projection residual blocks. Thus, it quickly moves features to the lowest resolution stages where it concentrates most of the heavy processing and leaves easier tasks for higher resolutions, efficiently balancing the computational complexity across scales. This is analogous to multigrid PDE solvers that are known to be optimal in the solution of large systems of equations [36].
- It allows a recursive configuration sharing parameters in all back-projection blocks leading to good results and very small number of parameters, or alternatively, a non-recursive configuration that leads to better performance and an increased number of parameters.
- It can be extended to use 3D-convolutions for video. This is due to the property that back-projection blocks do not change the size of the input and allows to learn a mapping from many input to many output frames. This is a convenient property that we call *Cube-to-Cube* and it leads to a fully 3D-convolutional network that we call MGBP-3D. It departs significantly from other video solutions mentioned above as it relies completely on 3D-convolutions and do not include other non-linear blocks such as attention, warping, dynamic filters or deformable convolutions.

Second, we designed a particular training strategy for perceptual super-resolution with the following contributions:

- We propose a strategy to control the perception-distortion trade-off as a transition from a high-fidelity target to perceptual target through a so called *innovation jump*.
- We drive the innovation process of our MGBP architecture (generator) by introducing random inputs at each resolution level. These inputs are manipulated by the network to

generate artificial details at different scales.

- We propose a so-called *variance-normalization and shift-correlator* (VN+SC) layer that provides meaningful features to a discriminator system based upon previous research on the statistics of natural images.
- We propose a *multiscale discriminator* for adversarial training. It is a configuration symmetric to the multi-scale up-scaler, therefore it is more effective for adversarial training. It can simultaneously evaluate several upscaling factors, resembling a Progressive GAN [37] in the sense that the optimizer can focus on smaller factors first and then work on larger factors.
- We propose a novel *noise-adaptive training strategy* that can avoid conflicts between reconstruction and perceptual losses, combining loss functions with different random inputs.

An early version of the MGBP architecture first appeared in the NTIRE 2018 challenge on image SR [38], together with Deep Back-Projection Networks (DBPN) [39]. Both DBPN and MGBP used similar back-projection residual blocks with DBPN achieving better results and winning this challenge with a two-level configuration mixing up/down-backprojections. The architecture of MGBP was later improved in [33] achieving state-of-the-arts results in high-fidelity SR for lightweight networks with small number of parameters. The training strategy for perceptual quality first appeared in PIRM 2018 achieving the **2nd best perceptual quality** in the Perceptual SR challenge [32]. We refer to these early configurations using small number of parameters as MGBP version 1 (MGBPv1). The architecture was later improved in [40] to allow a non recursive structure that is more flexible and simple to configure, allowing a larger amount of parameters while at the same time being able to process very large images (e.g. 8K). This configuration was named MGBP version 2 (MGBPv2) and has won the **1st place for best perceptual quality** in the AIM 2019 challenge for Extreme Super-Resolution (16× factor) as well as **3rd best perceptual quality** in NTIRE 2020 challenge on Real-World Image SR. Here, we include new experiments to show that MGBPv2 can also achieve state-of-the-arts results in high-fidelity targets for image SR. Finally, we show how to extend MGBPv2 to the fully 3D-convolutional network MGBP-3D. This new architecture was recently used in the AIM 2020 Video Extreme Super-Resolution Challenge achieving the **2nd best fidelity** [30]. Overall, the MGBP architecture has been particularly successful as a convenient configuration to balance multi-scale computational complexity for large upscaling factors in both image and video SR as well as achieving state-of-the-arts results in perceptual super-resolution.

II. PERCEPTUAL AND DISTORTION TARGETS

To better illustrate our target, we present a diagram of image sets in Figure 2. Here, \mathcal{H} is the set of all high-resolution images, $\mathcal{H}^{real} \subset \mathcal{H}$ is the subset of high-resolution images that correspond to natural images, and \mathcal{L} is the set of all low-resolution images. Given an image $X \in \mathcal{H}^{real}$, we are interested in the set of *aliased* images:

$$\mathcal{A}(X) = \{Y \in \mathcal{H} \quad s.t. \quad S_f(Y) = S_f(X)\}, \quad (1)$$

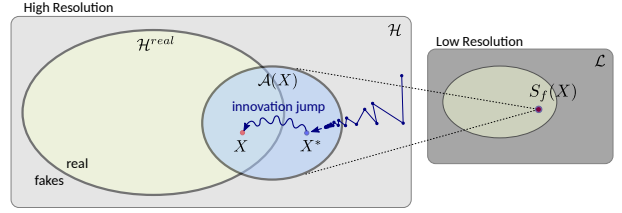


Fig. 2. For a high-resolution image X that looks real, distortion optimization approaches an optimal solution X^* that does not look real because it lacks the unpredictable nature of natural images. We can still use X^* as a reference point to move through an *innovation jump* into the set of realistic images.

where $S_f : \mathcal{H} \rightarrow \mathcal{L}$ is a *downscale* operator of factor f . We are particularly interested in the set $\mathcal{A}(X) \cap \mathcal{H}^{real}$ of alias images that correspond to real content.

A *distortion* function $\Delta(X, y)$ measures the dissimilarity between a reconstructed image y and the original image X . Popular and basic distortion metrics such as L1, L2, PSNR, etc., are sensitive to changes (any minor difference in pixel values would increase the amount of distortion) and are known to have low correlation with human perception [41]. Several distortion metrics have been proposed to approach perceptual quality by emphasizing some differences more than others, either through normalization, feature extraction or other approaches. These include metrics like SSIM [42], VIF [43] and the VGG content loss [44]. By doing so, correlation with human perception improves according to [41], but experiments in [31] show that these metrics still focus more on distortion. More recently, the contextual loss has been proposed to focus more on perceptual quality while maintaining a reasonable level of distortion [45].

The solution of distortion optimization is obtained by:

$$X^* = \operatorname{argmin}_y \mathbb{E}[\Delta(X, y)] . \quad (2)$$

The original image X is fixed, and the expected value in (2) removes any visible randomness in the search variable y . But, according to research on the statistics of natural images, randomness plays an essential role in what makes images look real [46]. This is well known for non-reference image quality metrics such as NIQE [47] or BRISQUE [48], and led to a definition of perceptual quality as a distance between probability distributions in [31]. It is also known that distortion optimization solutions tend to look unreal, as seen in state-of-the-art results from NTIRE-SR Challenges [38], [49]. Common distortion metrics in these challenges (L1 and L2) make the image X^* lose all randomness. We argue that this removal of randomness in X^* is what moves it out of set \mathcal{H}^{real} , as we show in Figure 2.

We know that $X \neq X^*$ because $X \in \mathcal{H}^{real}$ and $X^* \notin \mathcal{H}^{real}$ according to our previous discussion. However, distortion optimization can still be useful to generate realistic images. By approaching X^* we are getting closer to X . As shown in Figure 2, both X and X^* can be in $\mathcal{A}(X)$. Using a signal processing terminology, the *innovation* [50] is the difference between X and the optimal forecast of that image based on prior information, X^* . Most SR architectures take the randomness for the innovation process from the low-resolution

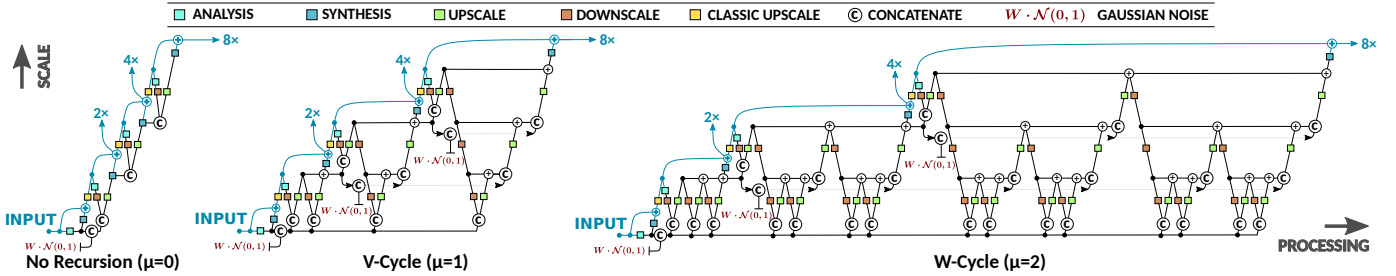


Fig. 3. Diagram of the MultiGrid BackProjection version 1 (MGBPv1) network [33] with $\mu = 0, 1,$ and $2.$

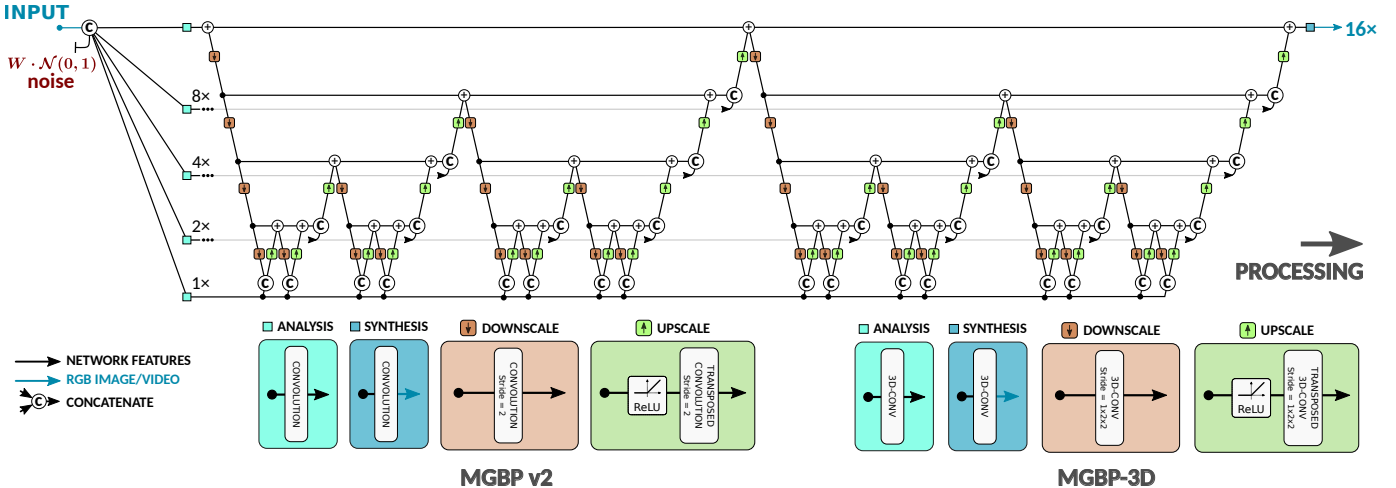


Fig. 4. Diagram of the MultiGrid BackProjection network version 2 (MGBPv2) for images and MGBP-3D for videos unfolded from Algorithm 1 with $\mu = 2.$

input image, which is a valid approach but loses the ability to expose and control it.

In our proposed architecture we add randomness explicitly as noise inputs, so that we can control the amount of innovation in the output. Independent and identically distributed noise will enter the network architecture at different scales, so that each of them can target artificial details of different sizes. Generally speaking, our training strategy will be to approach X^* with zero input noise and any image in $\mathcal{A}(X) \cap \mathcal{H}^{real}$ with unit input noise. By using noise to target perceptual quality, and remove it for the distortion target, we teach the network to *jump* from X^* into \mathcal{H}^{real} . With probability one the network cannot hit X , but the perceptual target is any image in $\mathcal{A}(X) \cap \mathcal{H}^{real}$.

III. ARCHITECTURE

A. Generator

Motivation. The general problem of image restoration is to recover an image X that has been degraded. This could mean that either some details have been removed from the image (e.g. blurring) or some new information is interfering and corrupting the image (e.g. noisy measurements). Here, we will focus on the problem of image super-resolution, assuming a degradation model of the form:

$$x = R(X), \quad (3)$$

where $X \in \mathbb{R}^N$ is the high-resolution source, $x \in \mathbb{R}^n$ is the low-resolution result, and $R : \mathbb{R}^N \rightarrow \mathbb{R}^n$ is a *restriction* operator (downscaler). A classic linear model is $R(X) = (X * g) \downarrow s$ where g is a blurring kernel (e.g. bicubic) and $\downarrow s$ is a downsampling by factor s dropping pixels to reduce the resolution.

The degradation model (3) represents a prior knowledge that we would like to enforce on our system, aiming to recover the original image. This is the motivation behind the classic Iterative Back-Projection (IBP) algorithm [51]. Given model (3) and an upscaled image y_0 , the IBP algorithm iterates:

$$e_k = x - R(y_k), \quad (4)$$

$$y_{k+1} = y_k + P(e_k). \quad (5)$$

Here, $e(y_k)$ is the mismatch error at low-resolution and $P : \mathbb{R}^n \rightarrow \mathbb{R}^N$ is a projection operator (upscaler). A classic linear projection is $P(x) = (x \uparrow s) * p$, where p is an upscaling filter (a convolution) and $\uparrow s$ is increasing the resolution by inserting zeros. For linear operators P and R , it is simple to see that y_k will follow the degradation model (3) as $k \rightarrow \infty$ when $\|I - RP\| < 1$ [51].

IBP computes a residual $P(e_k)$ to update the output in successive iterations. It is thus natural to think of this process as a residual block. The restriction operator R can be implemented with a strided convolutional layer and the projection

Algorithm 1 Multi-Grid Back-Projection version 2 (MGBPv2)

MGBPv2(X, W, μ, L):

Input: Input image X .

Input: Steps μ , levels L and noise amplitude W .

Output: Output image Y .

```

1:  $x = [X, W \cdot \mathcal{N}(0, 1)]$ 
2: for  $k = 1, \dots, L$  do
3:    $y_k = \text{Analysis}_k(x)$ 
4: end for
5: for  $k = 1, \dots, L$  do
6:    $\text{tag}_k = 0$ 
7: end for
8:  $y = \text{BP}_L^\mu(y_L | y_1, \dots, y_{L-1}; \text{tag}_1, \dots, \text{tag}_{L-1})$ 
9:  $Y = \text{Synthesis}(y)$ 

```

 BP_k^μ ($u | y_1, \dots, y_{k-1}; \text{tag}_1, \dots, \text{tag}_{k-1}$):

Input: Input image u , level index k , steps μ .

Input: Images y_1, \dots, y_{k-1} and $\text{tag}_1, \dots, \text{tag}_{k-1}$ (for $k > 1$).

Output: Image out

```

1:  $out = u$ 
2: if  $k > 1$  then
3:   for  $s = 1, \dots, \mu$  do
4:      $\text{tag}_{k-1} = s$ 
5:      $LR = \text{Downscale}_{\text{tag}}(out)$ 
6:      $c = \text{BP}_{k-1}^\mu(LR | y_1, \dots, y_{k-2}; \text{tag}_1, \dots, \text{tag}_{k-2})$ 
7:      $out = out + \text{Upscale}_{\text{tag}}([y_{k-1}, c])$ 
8:   end for
9: end if

```

operator P with a strided transposed convolution. In MGBP we use these residual steps and follow the design of residual blocks in EDSR [11] by using a single rectified linear unit just before the transposed convolution in the P operator. We also make a small generalization by changing the error equation (4) to $e_k = [x, R(y_k)]$ where $[\cdot, \cdot]$ replaces the difference to concatenation of features (in the channel dimension). The projector operator P will then decide how to compare x and $R(y_k)$ in the update equation (5).

The IBP iteration does work as a residual block but it is different to the conventional blocks used in ResNets [10] in that IBP performs the correction at a lower resolution. This is similar to the way a Full-Multigrid algorithm solves linear equations [36]. That is: first, find an approximate solution in a small grid; and second, interpolate the approximate solution to update the solution in a large grid. Here, we borrow an essential idea of multigrid methods, that is to repeat the process recursively with residual backprojection blocks within residual backprojection blocks that quickly move features the lowest resolutions. Hence, two step back-projection residuals in high resolution ($\mu = 2$) leads to 4 residual steps in the next lower resolution, 8 in the next level, and so forth. The pattern unfolded is known in multigrid literature as a W-cycle [36] as seen in Figure 3.

The MGBP algorithm has been updated from version 1 (MGPBv1) in [33] to version 2 (MGPBv2) in [35] but the core idea explained above has remained unchanged. The latest Multi-Grid Back-Projection algorithm (MGBPv2) is shown in Figure 4 that follows from Algorithm 1.

Cube-to-Cube property. When we upscale sequences of images that come from video streams it is well known that temporal information plays a crucial role. Independently super-resolving frames loses important temporal correlations and introduces temporal artifacts such as flickering. A simple model to add this information is to interpret time as an extra dimension. In this interpretation flickering artifacts are the temporal version of jaggies in space. We can visualize the spatio-temporal information of a video clip in a cubical arrangement of pixels as seen in Figure 5-a. The cross sections of the cube along temporal dimension reveal a smooth continuity of pixel value changes across time. A common solution for video super-resolution is to use 3D convolutions to extract this information based on the fact that these cross

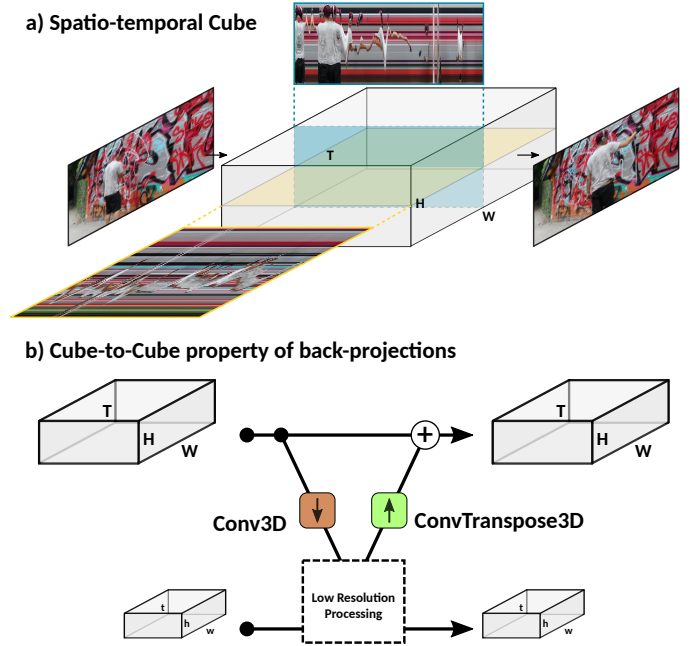


Fig. 5. a) A video clip is represented as a spatio-temporal cube. b) A back-projection module using a convolution and transposed convolution with same kernel size preserve the dimensions of the cube. Padding is no needed and can reduce the memory footprint at low resolution levels.

sections share strong similarities with 2D images (eg. sharp and smooth edges).

Extending a network model from 2D to 3D convolutions is particularly simple when using back-projections because of the property shown in Figure 5-b. As we already know, a back-projection module uses a strided convolution to move down in scale and strided transposed convolution to move back. Here, we assume that both convolution and transposed convolutions use the same kernel sizes and padding settings. Because the matrix representation of this transposed convolution has the same dimensions of the transposed matrix for its convolution counterpart, the residual update in the back-projection module has the exact same resolution as the initial state. This remains true with or without padding in the convolutional modules. We call this the *Cube-to-Cube* property of back-projection modules. The property holds for any number

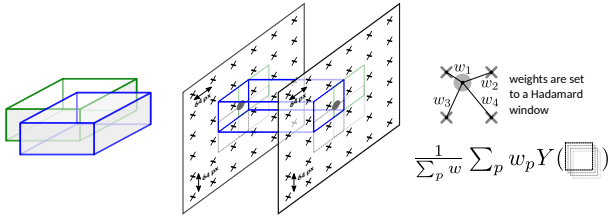


Fig. 6. For video inference, using a fully 3D-convolutional architecture such as MGBP-3D is more difficult than image since in practice we are unable to input a 3D-cube with the entire video sequence. We solve this issue by using overlapping 3D-patches that are averaged using a Hadamard window.

of dimension (e.g. using 1D, 2D or 3D convolutions) but it is particularly useful for higher dimensions. This is because by removing padding we save a fix amount of pixels in 1D, a fix amount of lines (rows or columns) in 2D, and a fix amount of images in 3D, without reducing the receptive field of convolutional layers. The memory saving becomes significant when processing video as we move down in scale using back-projection blocks. For example, we used 37 frames to train a $1 \times 16 \times 16 \times$ MGBP-3D (scaling in space and not in time) that became 29 frames at the lowest resolution of the network when using kernel size 3 in time and no padding, compared to 37 frames with padding. The volume saving at the lowest resolution is $\sim 22\%$ which allows us to use a large number of features (256). This is a clear advantage of using a fully 3D-convolutional network structure.

Video Inference. To upscale large video sequences we propose a patch based approach in which we average the output of overlapping video patches taken from the bicubic upscaled input. First, we divide input streams into overlapping patches (of same size as training patches) as shown in Figure 6; second, we multiply each output by weights set to a Hadamard window; and third, we average the results. In our experiments we use overlapping patches separated by 5 video frames.

This strategy is necessary for video as we cannot input a spatio-temporal cube with the complete input sequence. This limitation of fully 3D-convolutional networks could be avoided if tensor processing frameworks implement *streaming 3D-convolutions* where output frames come out as input frames arrive, using a FIFO structure equivalent to the implementation of audio filters.

Generator Architecture. Algorithm 1 refers to the second version of MGBP [35]. One of the differences between the first and second versions is the initialization step. Without loss of generality, in the second version we tackled the image enhancement problem with an input resolution equal to the output resolution. For the super-resolution task we input the low resolution image upscaled using a bicubic method. This helps to make the system become more general for applications and simplifies the process of generating pairs of input/output patches during training. In contrast, the first version MGBPv1 shown in Figure 3 started at the lowest resolution and progressively upscaled the input with a bicubic upscaler, entering the multigrid cycle at different resolutions.

Figure 4 displays the diagram of the MGBPv2 algorithm unfolded for $\mu = 2$ and $L = 5$. The *Analysis* and *Synthesis*

modules convert an image into feature space and vice-versa using single convolutional layers. The *Upscaler* and *Downscaler* modules are composed of single strided (transposed and conventional) convolutional layers. An important observation in Algorithm 1 is the use of a `tag` label to differentiate each *Upscaler* and *Downscaler* module. This simple trick was introduced in MGBPv2 and makes every *Upscaler* and *Downscaler* module different in terms of parameters and hyper-parameters. In particular, we can now set a different number of features in convolutional layers from low to high resolution levels, allowing large images to be processed at high resolutions by using small number of features and increase it at lower resolutions. The system can be initialized by a *dry run* of Algorithm 1 where no computation is performed and modules are defined with their correspondent `tag` labels. The MGBPv1 system did not include this feature and it was forced to use identical *Upscaler* and *Downscaler* in all instances of these modules. In this case a single convolutional layer would not give good results and 4-layer DenseNets were used inside these modules [33].

The same diagram for MGBPv2 in Figure 4 represents the architecture of MGBP-3D and the same Algorithm 1 is used for video SR. The difference between MGBPv2 and MGBP-3D is in the configuration of the *Analysis*, *Synthesis*, *Upscaler* and *Downscaler* modules that now used 3D-convolutions as shown in Figure 4. This simple extension is due to the *Cube-to-Cube* property explained above.

Complexity. The W-cycle pattern shown in Figure 4 is unfolded when using $\mu = 2$, and it is also a popular configuration in multigrid methods [36]. Let $f(n)$ be the computational complexity of the residual backprojection module in a resolution of $n = H \times W$ pixels. For example, $f(n) = \mathcal{O}(n^{1/2})$ if we use the same *Upscaler* and *Downscaler* modules all over the network. Then, the number of products $p(n)$ at resolution n using MGBP obeys the recurrence relation:

$$p(n) = f(n) + \mu \cdot p(n/4), \quad (6)$$

assuming a downscaling by factor 2×2 (horizontal and vertical). The solutions of this recurrence are known as the master theorem for divide-and-conquer [52]. In MGBPv1 we have $f(n) = \mathcal{O}(n^{1/2})$ and $\mu = 2$, that leads to a computational complexity $p(n) = \mathcal{O}(n \log n)$. This is inconvenient in practice and it made it impossible, for example, to apply MGBPv1 in the Extreme-SR AIM 2019 challenge with upscaling factor $16\times$ and 8K output resolution. The complexity can be reduced to $\mathcal{O}(\log n)$ if we manipulate the *Upscaler* and *Downscaler* modules such that $f(n) = \mathcal{O}(n^{1/2-\epsilon})$ for some $\epsilon > 0$. This is easily achieved by both MGBPv2 and MGBP-3D by reducing the number of features per level in convolutional layers as a function of n .

In terms of memory requirements the resolution of feature maps decreases by factor $2 \times 2 = 4$ at each scale (using stride 2 in *Upscaler* and *Downscaler* modules). All versions of MGBP need to keep one copy of the feature map at each scale (similar to UNets) and the geometric sum of pixel counts from different scales leads to $\mathcal{O}(n)$. Therefore, MGBP memory footprint scales correctly by linearly increasing the memory requirements as the number of pixels increases.

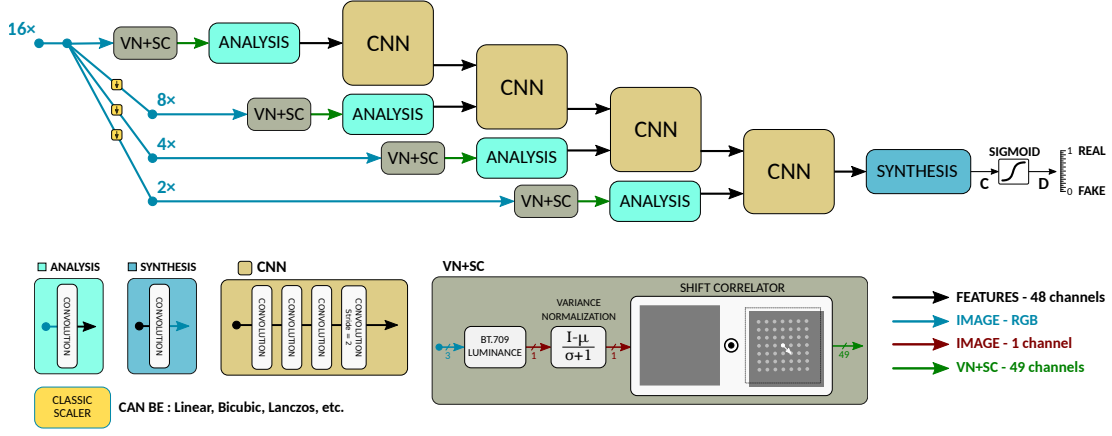


Fig. 7. Discriminator system used for adversarial training. The high resolution input image is downsized with standard bicubic downscalers to enter the system at different scales. CNN modules do not share parameters. Only image content is considered for adversarial training as the temporal evolution of artificial details required for videos makes the problem significantly more difficult and currently unresolved.

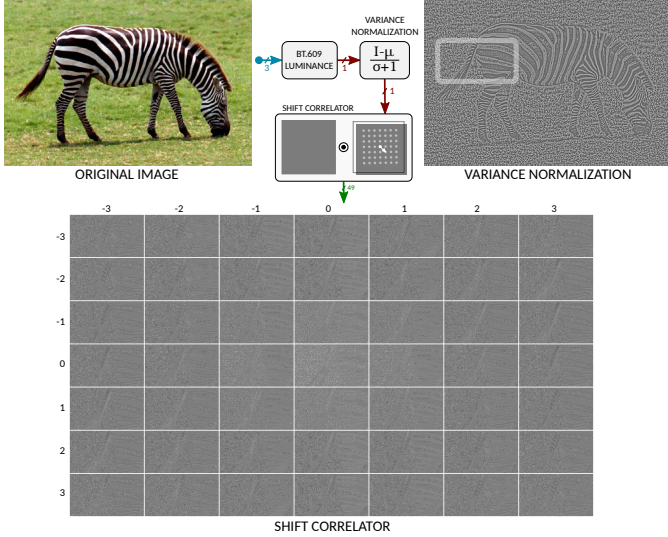


Fig. 8. Our VN+SC layer considers the luminance channel of a color image (using the BT.609 standard for conversion from RGB), applies variance normalization (upper right image), and computes the Hadamard product with its shift versions (bottom image showing only outputs for the white box in variance normalization image). We use these 49 channels as inputs of the Discriminator.

B. Discriminator

The task of the discriminator is to measure how realistic is an image or video frame. A straightforward approach is to input the color image to a sequential convolutional network architecture. Then, we hope that the discriminator learns from adversarial training using real and fake image examples. In practice, we find that this approach works well to identify which areas of upscale images need more textures but the artificial details look noisy and have limited structure.

So what makes an image look natural? Extensive research has been carried to address this question. Here, we follow the seminal work of Ruderman [46] who found regular statistical properties in natural images that are modified by distortions. In particular, Ruderman observed that applying the so-called

variance normalization operation:

$$\hat{I}_{i,j} = \frac{I_{i,j} - \mu_{i,j}(I)}{\sigma_{i,j}(I) + 1}, \quad (7)$$

has a decorrelating effect on natural images. Here, $I_{i,j}$ is the luminance channel of an image with values in $[0, 255]$ at pixel (i, j) , $\mu(I)$ is the local mean of I (e.g. output of a Gaussian filter), and $\sigma(I)^2 = \mu(I^2) - \mu^2(I)$ is the local variance of I . Ruderman also observed that these normalized values strongly tend towards a Gaussian characteristic for natural images. These findings are used in the NIQE perceptual quality metric considered for the PIRM-SR Challenge 2018 [47]. NIQE also models the statistical relationships between neighboring pixels by considering horizontal and vertical neighbor products: $\hat{I}_{i,j}\hat{I}_{i,j+1}$, $\hat{I}_{i,j}\hat{I}_{i+1,j}$, $\hat{I}_{i,j}\hat{I}_{i,j-1}$ and $\hat{I}_{i,j}\hat{I}_{i-1,j}$.

Variance Normalization and Shift Correlator (VN+SC). Inspired by previous research we define the Variance Normalization and Shift Correlator (VN+SC) layer as follows:

$$V_{i,j}^{7(p+3)+q+3}(I) = \hat{I}_{i,j} \cdot \hat{I}_{i+p,j+q}, \quad \begin{matrix} p = -3, \dots, 3, \\ q = -3, \dots, 3. \end{matrix} \quad (8)$$

Here, we transform a color image into a set of neighbor products (shift correlator) $V_{i,j}^k$ with $k = 0, \dots, 48$, using the variance normalized image \hat{I} . The Gaussian filter used for local mean and variance is set to have kernel size 7×7 and $\sigma = 1.17$ based on similar values used in NIQE [47]. The number of neighbor products is an additional parameter that we set to 7×7 that is a number larger than 3×3 used in NIQE and BRISQUE and close to 64 that is the number of features used in the discriminator architecture. The luminance channel is obtained using the BT.609 color matrix following the implementation of NIQE [47].

Figure 8 shows the visual effect of the the VN+SC operation. A zoom on the tail of a zebra shows a visible correlation along the tail and less so in the stripes of the zebra. We use a VN+SC layer for each input of our discriminator, as shown in Figure 7. This reduces the amount of information received by the discriminator and, in particular, removes all color information. This follows closely the empirical findings

of Ruderman [46] to determine if an image looks natural. Color information will be considered by other terms of the loss function.

Discriminator Architecture. For the discriminator in adversarial training we use the system shown in Figure 7. Here, we use 4-layer sequential CNNs with 3×3 filters and stride 1 except for the last layer that uses stride 2 to downscale the features. The discriminator used with MGBPv1 in [34] had two minor differences: first, the CNNs shared parameters making the system recursive (imitating MGBPv1); and second, the progressive outputs of MGBPv1 entered the discriminator at different stages. Adversarial training with this discriminator resembles a Progressive GAN [37] because it can adjust parameters to first solve the simpler problem of $2 \times$ upscaling, and then follow with larger factors. But, at the same time, it is significantly different because a Progressive GAN system is neither multi-scale nor recursive. Overall, the major properties of our discriminator architecture, both for MGBPv1 and MGBPv2, are: input the RGB output of the generator in different resolutions (high resolution enter first, lower resolutions enter later); and, RGB images are converted into $49 = 7 \times 7$ channels with the VN+SC modules. A 3D-convolutional version of the discriminator was used for video content in the AIM 2020 Video Extreme Super-Resolution Challenge [30] but did not succeed to achieve the same realistic effect observed in images. The temporal evolution of artificial details required for videos makes the problem significantly more difficult and currently unresolved. Therefore, here we will only consider the adversarial training strategy for image content.

IV. LEARNING

A. Configurations

In the first version of MGBP (MGBPv1) the *Analysis*, *Synthesis*, *Upscale*, *Downscale* and *CNN-discriminator* modules used 4-layer dense networks [12] with a correspondent strided convolutional or transposed convolutional layer for downscale or upscale operations, respectively. We used 48 features and growth rate 16 within dense networks. For classic upscaler we configured a Bicubic and we set the upscaling filters as parameters to learn as proposed in [53].

In the second version, MGBPv2, the *Analysis*, *Synthesis*, *Upscale*, *Downscale* were configured with single convolutional layers. Here, we used different configurations depending on the upscaling factor. Table I–a shows the number of levels, the parameter μ and the number of convolutional layer features used for each upscaling factor. For small upscaling factors (2 and 3) we chose a configuration almost equivalent to EDSR [11] with only two levels and 32 residual back-projection blocks.

For MGBP-3D the *Analysis*, *Synthesis*, *Upscale*, *Downscale* were configured using single 3D-convolutional layers as shown in Figure 4. Similar to MGBPv2, we used different configurations depending on the upscaling factors $4 \times$ and $16 \times$. Table I–b shows the number of levels, the parameter μ and the number of convolutional layer features used for each upscaling factor.

For perceptual quality we concatenate a single noise channel, $W \cdot \mathcal{N}(0, 1)$, to the bicubic upscaled input in MGBPv2

TABLE I
MGBPv2 AND MGBP-3D NETWORK CONFIGURATIONS. HIGH-FIDELITY PERFORMANCE IS SHOWN IN TABLES II AND IV.

	Factor	μ	Levels	Channels per level
a) MGBP-v2:	2	32	2	192-128
	3	32	2	192-128
	4	4	4	192-128-64-32
	8	2	5	192-128-64-32-16
	16	2	6	256-192-128-92-48-9
b) MGBP-3D:	Factor	μ	Levels	Channels per level
	4	6	4	192-128-64-32
	16	2	6	256-192-128-92-48-9

and the input at each resolution level in MGBPv1 as shown in Figures 3 and 4. The amplitude of the noise, $W \in \mathbb{R}$, is set to zero for high-fidelity targets and its purpose is to help in the adversarial training for perceptual quality. The noise activates and deactivates the generation of artificial details. In MGBPv1 [34], different i.i.d. noise channels are generated at each resolution. In MGBPv2 we generate a single noise channel at the highest resolution, that moves along with the input image to enter the network at different scales by using *Analysis* modules with different strides and becomes more simple to manipulate.

We denote $Y_{W=0}$ and $Y_{W=1}$ the outputs of the generator architecture using noise amplitudes $W = 0$ and $W = 1$, respectively. In all the experiments and challenges that we present here, a high-resolution image has been resized using a bicubic downscaler. Let S_f represent a bicubic downscaler that reduces the resolution by a factor $f \times f$ (horizontal and vertical). We would like our output Y to be such that $S_f(X) = S_f(Y)$ where X is the ground truth image. This is a prior knowledge that we will enforce in our loss functions during optimization.

B. Learning High Fidelity

We use $\mathcal{L}^{L1}(x, y) = \mathbb{E}[|x - y|]$ at several resolutions to define the total loss function:

$$\mathcal{L}(Y, X; \theta) = \mathcal{L}^{L1}(Y_{W=0}, X) + \sum_{k \in \{2, 4, \dots, f\}} \mathcal{L}^{L1}(S_k(Y_{W=0}), S_k(X)). \quad (9)$$

The first term is our main target, this is, to recover the high-resolution image. The sum over downscaling factors is meant to progressively give easier targets and enforce the downscaling model. After every epoch we evaluate the current model using $\mathcal{L}^{L2}(x, y) = \mathbb{E}[(x - y)^2]$ in the validation metric:

$$\mathcal{V}(Y; \theta) = \mathcal{L}^{L2}(Y_{W=0}, X). \quad (10)$$

We recorded the best models according to this metric (directly related to PSNR) during the training process.

The input X represents a 2D image or a 3D spatio-temporal cube for video content. In both MGBP-v2 and MGBP-3D the input X correspond to the bicubic upscaled content with the same resolution as the output Y . For video content this means that the network learns to map a number of input frames to the

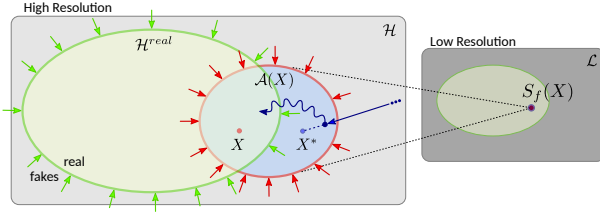


Fig. 9. Our loss function tries to: look real by moving into \mathcal{H}^{real} (GAN and CX loss), enforce a downscaling model by moving into $\mathcal{A}(X)$, and be reachable by latent space interpolation from the optimal distortion solution X^* (distortion loss).

same number of output frames. This is significantly different than the many-to-one frame mapping approach commonly used for video SR training and it is a consequence of the *Cube-to-Cube* property of MGBP-3D.

C. Learning Perceptual Quality

For perceptual training we use a generative adversarial approach, alternating training steps for the generator and the discriminator, following the Relativistic GAN from [54]. For total loss we use the following expression:

$$\begin{aligned} \mathcal{L}(Y, X; \theta) = & 0.001 \cdot \mathcal{L}_G^{RSGAN}(Y_{W=1}) + \\ & 10 \cdot \frac{1}{|C|} \sum_{k \in C} \mathcal{L}^{L^1}(S_k(Y_{W=1}), S_k(X)) + \\ & 0.1 \cdot \mathcal{L}^{CX}(Y_{W=1}, X) + \\ & 10 \cdot \mathcal{L}^{L^1}(Y_{W=0}, X) + \\ & 10 \cdot \frac{1}{|C|} \sum_{k \in C} \mathcal{L}^{L^1}(S_k(Y_{W=0}), S_k(X)), \quad (11) \end{aligned}$$

where the color is associated with the targets displayed in Figure 9 and $C = \{2, 4, \dots, f\}$ is the set of upscaling factors. This is, green losses try to enter the set of real images with $Y_{W=1}$; red losses try to enter the set of aliased images with both $Y_{W=1}$ and $Y_{W=0}$; and, blue losses try to recover the ground truth high-resolution image with $Y_{W=0}$.

The red losses in (11) enforcing the downscale model are also refer here as *cycle* losses. This is because the output images are brought back to the input domain for comparison with the original input.

In particular, \mathcal{L}^{CX} is the *contextual loss* as defined in [45] using features from *conv3-4* of a VGG-19 network as suggested in [55]. Ablation tests performed in the next section show the effectiveness of this loss function to improve perceptual quality while maintaining a reasonable level of distortion. Next, the Relativistic GAN loss follows the definition in [54], given by:

$$\begin{aligned} \mathcal{L}_D^{RSGAN} &= -\mathbb{E}_{(R,F)} [\log(\text{sigmoid}(C(R) - C(F)))] , \\ \mathcal{L}_G^{RSGAN} &= -\mathbb{E}_{(R,F)} [\log(\text{sigmoid}(C(F) - C(R)))] . \quad (12) \end{aligned}$$

Here, C is the output of the discriminator before the sigmoid function, as shown in Figure 7. And R and F are the sets of real and fake inputs to the discriminator, given by:

$$\begin{aligned} F &= \{Y_{W=1}, S_2(Y_{W=1}), S_4(Y_{W=1}), \dots\} , \\ R &= \{X, S_2(X), S_4(X), \dots\} . \quad (13) \end{aligned}$$

TABLE II
QUANTITATIVE EVALUATION OF MGBPv1 AND MGBPv2 FOR IMAGE SUPER-RESOLUTION WITH HIGH-FIDELITY TARGET.

Algorithm	Set14		BSDS100		Urban100		Manga109	
	PSNR	SSIM	PSNR	SSIM	PSNR	SSIM	PSNR	SSIM
Bicubic	30.34	0.870	29.56	0.844	26.88	0.841	30.84	0.935
A+ [56]	32.40	0.906	31.22	0.887	29.23	0.894	35.33	0.967
FSRCNN [57]	32.73	0.909	31.51	0.891	29.87	0.901	36.62	0.971
SRCNN [9]	32.29	0.903	31.36	0.888	29.52	0.895	35.72	0.968
MSLapSRN [53]	33.28	0.915	32.05	0.898	31.15	0.919	37.78	0.976
VDSR [58]	32.97	0.913	31.90	0.896	30.77	0.914	37.16	0.974
LapSRN [59]	33.08	0.913	31.80	0.895	30.41	0.910	37.27	0.974
DRCN [60]	32.98	0.913	31.85	0.894	30.76	0.913	37.57	0.973
D-DBPN [39]	33.85	0.919	32.27	0.900	32.70	0.931	39.10	0.978
EDSR [11]	33.92	0.919	32.32	0.901	32.93	0.935	39.10	0.977
RDN [61]	34.28	0.924	32.46	0.903	33.36	0.939	39.74	0.979
RCAN [15]	34.12	0.921	32.41	0.903	33.34	0.938	39.44	0.979
MGBPv1 [33]	33.27	0.915	31.99	0.897	31.37	0.920	37.92	0.976
MGBPv2	34.18	0.922	31.70	0.887	33.31	0.936	39.42	0.978
<hr/>								
Bicubic	27.55	0.774	27.21	0.739	24.46	0.735	26.95	0.856
SRCNN [9]	29.30	0.822	28.41	0.786	26.24	0.799	30.48	0.912
MSLapSRN [53]	29.97	0.836	28.93	0.800	27.47	0.837	32.68	0.939
LapSRN [59]	29.87	0.832	28.82	0.798	27.07	0.828	32.21	0.935
EDSR [11]	30.52	0.846	29.25	0.809	28.80	0.865	34.17	0.948
RDN [61]	30.74	0.850	29.38	0.812	29.18	0.872	34.81	0.951
MGBPv2	30.60	0.845	29.10	0.803	29.15	0.866	34.31	0.947
<hr/>								
Bicubic	26.10	0.704	25.96	0.669	23.15	0.659	24.92	0.789
A+ [56]	27.43	0.752	26.82	0.710	24.34	0.720	27.02	0.850
FSRCNN [57]	27.70	0.756	26.97	0.714	24.61	0.727	27.89	0.859
SRCNN [9]	27.61	0.754	26.91	0.712	24.53	0.724	27.66	0.858
MSLapSRN [53]	28.26	0.774	27.43	0.731	25.51	0.768	29.54	0.897
VDSR [58]	28.03	0.770	27.29	0.726	25.18	0.753	28.82	0.886
LapSRN [59]	28.19	0.772	27.32	0.728	25.21	0.756	29.09	0.890
DRCN [60]	28.04	0.770	27.24	0.724	25.14	0.752	28.97	0.886
D-DBPN [39]	28.82	0.786	27.72	0.740	26.54	0.795	31.18	0.914
EDSR [11]	28.80	0.788	27.71	0.742	26.64	0.803	31.02	0.915
RDN [61]	29.01	0.791	27.85	0.745	27.01	0.812	31.74	0.921
RCAN [15]	28.87	0.789	27.77	0.744	26.82	0.809	31.22	0.917
MGBPv1 [33]	28.43	0.778	27.42	0.732	25.70	0.774	30.07	0.904
MGBPv2	29.00	0.790	27.87	0.745	27.08	0.820	31.45	0.917
<hr/>								
Bicubic	23.19	0.568	23.67	0.547	20.74	0.516	21.47	0.647
A+ [56]	23.98	0.597	24.20	0.568	21.37	0.545	22.39	0.680
FSRCNN [57]	23.93	0.592	24.21	0.567	21.32	0.537	22.39	0.672
SRCNN [9]	23.85	0.593	24.13	0.565	21.29	0.543	22.37	0.682
MSLapSRN [53]	24.57	0.629	24.65	0.592	22.06	0.598	23.90	0.759
VDSR [58]	24.21	0.609	24.37	0.576	21.54	0.560	22.83	0.707
LapSRN [59]	24.44	0.623	24.54	0.586	21.81	0.582	23.39	0.735
D-DBPN [39]	25.13	0.648	24.88	0.601	22.83	0.622	25.30	0.799
EDSR [11]	24.94	0.640	24.80	0.596	22.47	0.620	24.58	0.778
RDN [61]	25.38	0.654	25.01	0.606	23.04	0.644	25.48	0.806
RCAN [15]	25.23	0.651	24.98	0.606	23.00	0.645	25.24	0.803
MGBPv1 [33]	24.82	0.635	24.67	0.592	22.21	0.603	24.12	0.765
MGBPv2	25.37	0.652	25.08	0.606	22.99	0.640	25.07	0.795

After every epoch we evaluated the current model according to the validation metric based on the NIQE [47] index:

$$\mathcal{V}(Y; \theta) = \mathbb{E} [NIQE(Y_{W=1})] . \quad (14)$$

This metric works as a simple rule to help identify models that generate realistic images in the full resolution.

V. PERFORMANCE

A. Fidelity Evaluation

In image SR we use DIV2K [62] and FLICKR-2K datasets for training and the following datasets for test: Set-14 [63], BSDS-100 [64], Urban-100 [65] and Manga-109 [66]. Impaired images were obtained by downscaling and then upscaling ground truth images, using bicubic scaler, with scaling factors: 2 \times , 3 \times , 4 \times and 8 \times . For evaluation we measure PSNR and SSIM on the Y-channel using the Matlab code from [67].

We follow the training settings from [11]. In each training batch, we randomly take 16 impaired patches from our training set (800 DIV2K plus 2,650 FLICKR-2K images). We consider both MGBPv1 and MGBPv2 models for each upscaling factor $f = 2, 4$ and 8. We use patch size $48f \times 48f$, for $f = 2, 3, 4$ and 8. We augment the patches by random horizontal/vertical flipping and rotating 90°. We use Adam

TABLE III
 QUANTITATIVE COMPARISON ON REDS4 FOR 4× VIDEO SUPER-RESOLUTION. MGBP-3D FRAMES CAN BE DOWNLOADED FROM [HERE](#).

Method	Clip_000		Clip_011		Clip_015		Clip_020		Average	
	PSNR	SSIM	PSNR	SSIM	PSNR	SSIM	PSNR	SSIM	PSNR	SSIM
Bicubic	24.55	0.6489	26.06	0.7261	28.52	0.8034	25.41	0.7386	26.14	0.7292
RCAN [29]	26.17	0.7371	29.34	0.8255	31.85	0.8881	27.74	0.8293	28.78	0.8200
TOFlow [25]	26.52	0.7540	27.80	0.7858	30.67	0.8609	26.92	0.7953	27.98	0.7990
DUF [26]	27.30	0.7937	28.38	0.8056	31.55	0.8846	27.30	0.8164	28.63	0.8251
EDVR [27]	28.01	0.8250	32.17	0.8864	34.06	0.9206	30.09	0.8881	31.09	0.8800
MGBP-3D	27.04	0.7793	29.11	0.8210	31.83	0.8855	27.77	0.8286	28.94	0.8286



Fig. 10. Qualitative evaluation of 16× video SR results from the AIM 2020 Video Extreme Super-Resolution Challenge [30]. MGBP-3D frames can be downloaded from [here](#).

optimizer [68] with learning rate initialized to 10^{-4} and decreased by half every 200,000 back-propagation steps.

Table II shows the performance at different upscaling factors. We observe that MGBPv2 performs very close to the best benchmarks, and performs better for large upscale factors 4× and 8×. MGBPv1 performance is lower than MGBPv2, but it is only outperformed by systems with large number of parameters like EDSR, DBPN, RDN, RCAN and MGBPv2. At small upscaling factors 2× and 3× we used an MGBPv2 configuration very similar to EDSR, with 32 residual blocks in two levels, but MGBPv2 clearly outperforms EDSR. This indicates the advantage of the residual back-projection block compared to conventional residual blocks. The multigrid recursion is effective in improving performance for large upscaling factors. It must be noted that the major trend in CNN architectures is to do all processing at low resolution and use PixelShuffle layers to quickly move to the highest resolution. MGBP balances this process by doing most work on the lowest resolutions and decrease the amount of work exponentially as it goes to

TABLE IV
 QUANTITATIVE RESULTS FOR AIM 2020 VIDEO EXTREME SUPER-RESOLUTION CHALLENGE (16×) [30].

Fidelity Rank	Team	PSNR	SSIM	Runtime	Perceptual Rank
1	KirinUK	22.83	0.6450	6.1s	1
2	MGBP-3D	22.48	0.6304	4.83s	4
2	Team-WVU	22.48	0.6378	4.90s	2
3	sr_xxx	22.43	0.6353	4s	5
4	ZZX	22.28	0.6321	4s	3
5	lyl	22.08	0.6256	13s	6
6	TTI	21.91	0.6165	0.249s	–
7	CET_CVLab	21.77	0.6112	0.04s	7
	Bicubic	20.69	0.5770		

higher resolutions.

In video SR we trained MGBP-3D using the REDS dataset [69] for 4× and Vid3oC [70] for 16× upscaling. In particular, for 4× we used the REDS4 configuration as specified in [27], training MGBP-3D with 266 video sequences and testing with 4 video sequences. Quantitative results are included in Table III. Here, MGBP-3D outperforms the image SR network RCAN [29] based on attention modules, the video SR network TOFlow [25] using optical flow estimation, and the video SR network DUF [26] using dynamic upscaling filters. But MGBP-3D is still far from the video SR network EDVR [27] using deformable convolutions. In extreme video SR (16×) we refer to the results of MGBP-3D in the AIM 2020 Challenge on Video Extreme Super-Resolution [30] with quantitative evaluations shown in Table IV and qualitative evaluations shown in Figure 10. Team KirinUK won the competition introducing EVESR-Net, using deformable convolutions for alignment and new attention modules [30]. MGBP-3D shared the 2nd place with Team-WVU that also used an architecture based on deformable convolutions. Overall, the result for both 4× and 16× indicate that MGBP-3D gains advantage compared to other methods for large upscale factors. The arrangement of the MGBP-3D architecture due to the multigrid strategy is particularly effective considering that the architecture only uses 3D-convolutions and ReLU units. This is in contrast to other methods using attention, deformable convolutions, warping or other non-linear modules.

B. Perceptual Evaluation

For image perceptual quality evaluations we refer to the results of MGBPv1 and MGBPv2 in the first challenge on perceptual image SR, PIRM-SR 2018 [32], and the first extreme SR challenge, AIM Extreme-SR 2019 [40], respectively.

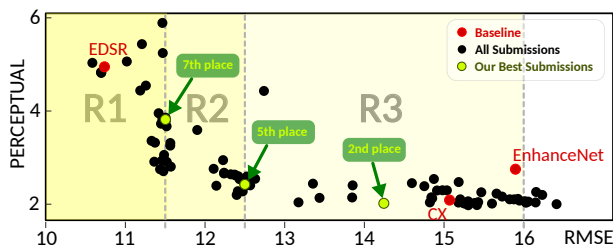


Fig. 11. Perception–distortion plane with average scores in the test set showing all submissions, from all teams in PIRM–SR 2018 [32]. Our best scores are shown in green color together with the final ranking in PIRM–SR Challenge 2018. The perception–distortion trade–off is clearly visible with an empty area in the lower–left corner.

Table V shows our best average scores and rankings in the PIRM–SR Challenge 2018 [32] for Region 1 ($RMSE \leq 11.5$), Region 2 ($11.5 < RMSE \leq 12.5$) and Region 3 ($12.5 < RMSE \leq 16$). Figure 11 shows all submissions in the perceptual–distortion plane, including the baseline methods: EDSR [11], CX [45] and EnhanceNet [71].

Compared to other submissions, we observe in Figure 11 that our system performs better in Region 3. Here, we achieve the 2nd place within very small differences in perceptual scores but with significantly lower distortion. This shows the advantage of our training strategy to optimize the perception–distortion trade–off. In Regions 1 and 2 we were one among only two teams that reached the exact distortion limit (11.5 in Region 1 and 12.5 in Region 2). We were able to achieve this by controlling the noise amplitude, without retraining the system. Our ranking lowers as the distortion target gets more difficult. We believe that this is caused by the small size of our system that becomes more important for low distortion targets, since we use only 281k parameters compared to 43M of the EDSR baseline in Region 1.

Figure 12 shows comparisons of our results with the baselines, using images from our validation set. We observe that in Region 3 we achieve better perceptual scores even compared to the original HR images. While we subjectively confirm this in some patches, we do not make the same conclusion after observing the whole images. Somehow, we believe that our design for adversarial training and validation strategy managed to overfit the perceptual scores. Nevertheless, we observe clear advantages to the baselines, showing better structure in textures and more consistent geometry in edges and shapes.

In the Perceptual track of the Extreme–SR AIM 2019 challenge our results using MGBPv2 obtained the 1st place in terms of a subjective ranking based on mean opinion scores (MOS) to measure perceptual quality. Our results obtained an average PSNR of 25.44 dB in the full output images of the test set. This is, 0.18 dB above the 2nd place and 1.35 dB below the best PSNR value in the Fidelity track.

Figure 13 shows two examples of our best results for the Fidelity and Perceptual tracks on images used for validation during our training process. These images show the values of RMSE (measuring fidelity) as well as the Perceptual index proposed in [32] to objectively measure perceptual quality. Overall, the results are consistent with the perception/distortion trade–off in [31]. For the image 622 we observe that our

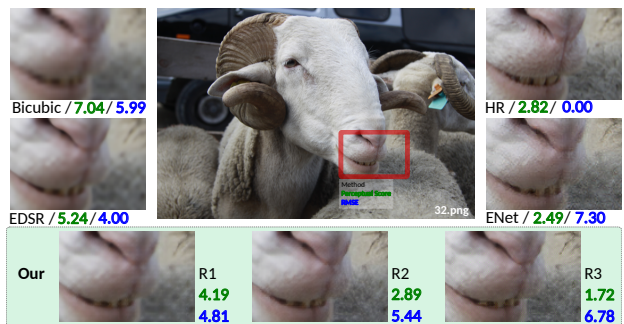


Fig. 12. PIRM–SR 2018 comparisons of 4 \times upscaling between our solutions in R1, R2 and R3 (see Figure 11) and baseline methods in our validation set. Perceptual and distortion scores of whole images are shown in green and blue colors, respectively.

results for the Perceptual track achieve a Perceptual index better than original image. We attribute this result to a blurred background in the original image, that our system shows more focused and with sharper features. For image 1466, the Perceptual index is clearly below those of the original image. According to our subjective evaluation, we observe clear differences in the fine level features like textbook spines. From a far away look these details become less perceptible, indicating that the Perceptual index correlates better with a close distance observer. This is probably caused by the resolution of example images used to adjust the Perceptual index, that are much smaller than 8K.

VI. ANALYSIS

A. Perception–Distortion Trajectory

An essential part of our generative SR architecture is the noise input. The training strategy introduced in Section II teaches the system to optimize distortion when the noise is set to zero, and maximize perceptual quality when the noise is enabled. Thus, noise provides the randomness needed for

TABLE V
PIRM 2018 CHALLENGE RESULTS. MOS TESTS WERE PERFORMED ONLY FOR TOP SUBMISSIONS [32].

Region 1					Region 2					Region 3				
Rank	Team	PI	RMSE	MOS	Rank	Team	PI	RMSE	MOS	Rank	Team	PI	RMSE	MOS
1	IPCV [72]	2.709	11.48	2.22	1	TTI [73]	2.199	12.40	2.17	1	SuperSR [74]	1.978	15.30	2.64
2	MCML [75]	2.750	11.44	1.87	2	IPCV [72]	2.275	12.47	2.43	2	MGBPv1 [34]	2.019	14.24	2.61
3	SuperSR [74]	2.933	11.50	2.19	2	MCML [76]	2.279	12.41	2.47	3	IPCV [72]	2.013	15.26	2.60
3	TTI [73]	2.938	11.46	1.88	4	SuperSR [74]	2.424	12.50	–	4	AIM [77]	2.013	15.60	–
5	AIM [77]	3.321	11.37	–	5	MGBPv1 [34]	2.484	12.50	–	5	TTI [73]	2.040	13.17	–
6	DSP-whu	3.728	11.45	–	6	AIM [77]	2.600	12.42	–	6	Haiyun [78]	2.077	15.95	–
7	MGBPv1 [34]	3.817	11.50	–	7	REC-SR [79]	2.635	12.37	–	7	gayNet	2.104	15.88	–
7	REC-SR [79]	3.831	11.46	–	8	DSP-whu	2.660	12.24	–	8	DSP-whu	2.114	15.93	–
9	Haiyun [78]	4.440	11.19	–	9	XYN	2.946	12.23	–	9	MCML	2.136	13.44	–

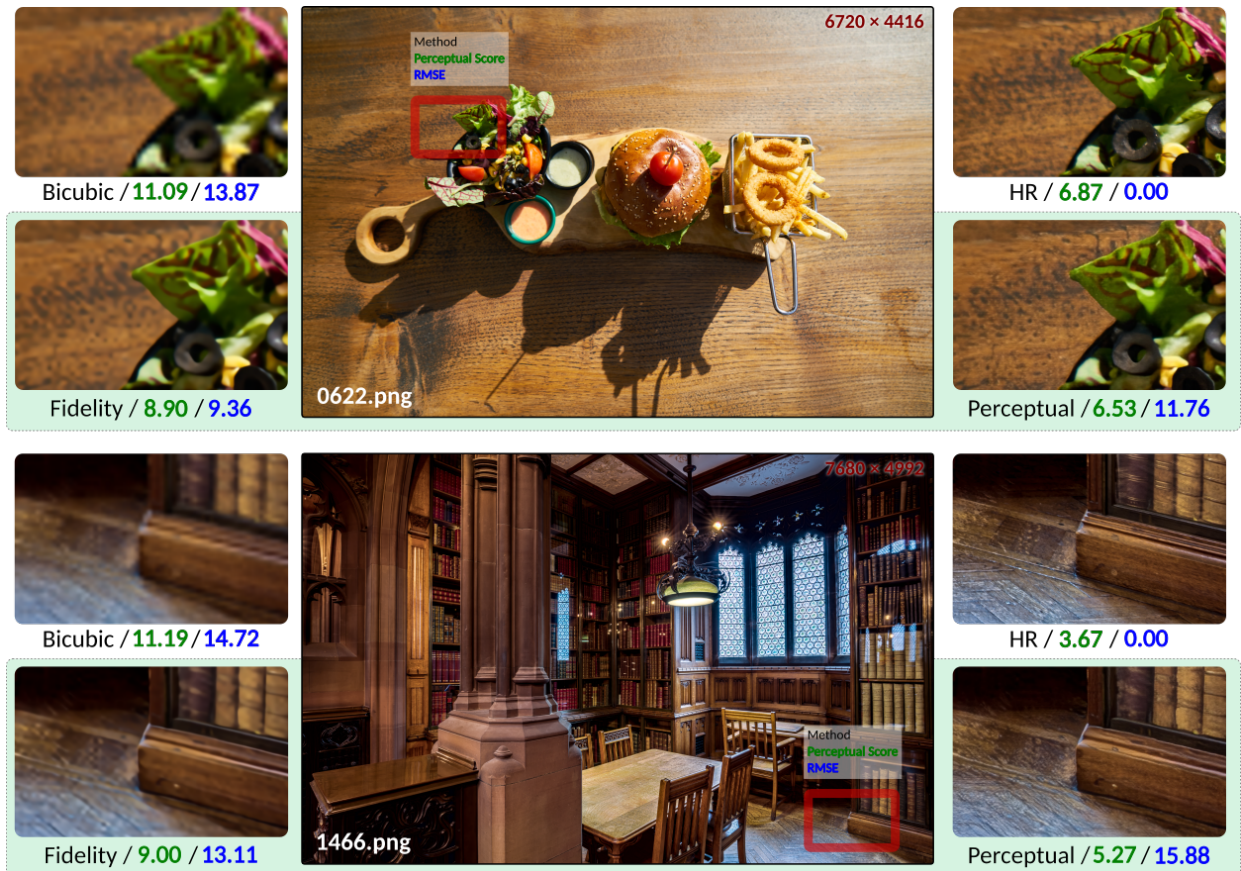


Fig. 13. Example outputs and performance metrics of our MGBPv2 16 \times model used for AIM Extreme-SR 2019 [40]. These images were selected from the DIV8K training set and we used them for validation purposes.

TABLE VI
AIM 2019 EXTREME SR CHALLENGE TRACK 2 PERCEPTUAL RESULTS
AND FINAL RANKINGS ON THE DIV8K TEST SET [40].

Rank	Team/Method	PSNR	SSIM	Runtime
1	MGBPv2	25.44	0.6551	47.11s
2	TTI	25.26	0.6523	80s
3	SRSTAR	26.72	0.7285	40s
4	SSRR	26.53	0.7246	40s

natural images and represents the *innovation jump* according to Figure 2.

After training, we are free to control the noise inputs. In particular, we can move the noise amplitude smoothly between $W = 0$ and $W = 1$ to inspect the path to jump

from distortion to perception optimization. Figure 14 shows an example of this transition. Our training strategy does not optimize the trajectory in the perception–distortion plane, but only the corner cases of best distortion ($W = 0$) and best perception ($W = 1$). The corner cases are clearly verified in Figure 14. At this point, it is unknown which trajectory will the network take to move from one case to the other.

It is interesting to see in Figure 14 that the transition from best perception to best distortion happens within a narrow margin of $\Delta W = 0.2$ amplitude values. We also observe that the parametric curve in the perception–distortion plane looks like a monotonically non-increasing and convex function, similar to the optimal solution studied in [31]. But, it is important to emphasize that the curve in Figure 14 is not

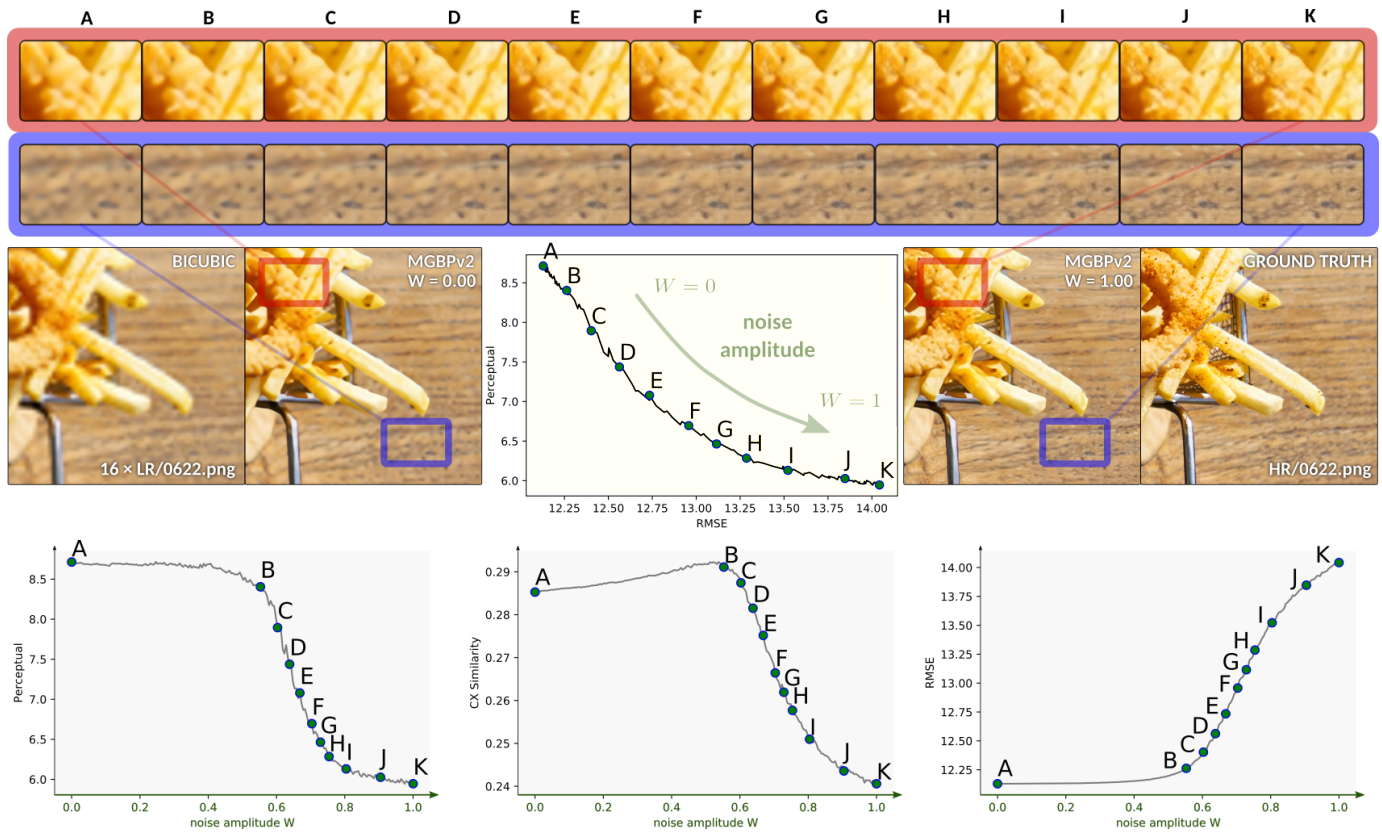


Fig. 14. Evolution of perceptual and fidelity metrics when moving the input noise amplitude from $W = 0$ to $W = 1$ in our MGBPv2 $16\times$ system used for AIM Extreme-SR 2019 [40].

optimal as we are not enforcing optimality. The results in Table V and Figure 11 clearly show that our perception–distortion curve, despite being concave, gets farther from optimality in low distortion regions.

Regarding image quality metrics, we see with no surprise that the *Perceptual* index proposed for the PIRM–SR Challenge [32] improves as noise increases, while the distortion measured by RMSE increases. We observed very similar results for the perceptual metrics NIQE and Ma, as well as the L1 distortion metric. More interesting is the transition observed in the *contextual similarity* index. First, it behaves as a perceptual score with the CX similarity improving consistently as noise increases. Then, when the *Perceptual* score seems to stall, but RMSE keeps increasing, the CX similarity changes to a distortion metric pattern, reducing as noise increases. This is consistent with the design target of CX similarity to focus more on perceptual quality while maintaining a reasonable level of distortion [45].

B. Ablation Tests

Our overall loss combines terms focused on different targets (e.g. low distortion, perceptual quality). In Section IV-B we explained the purpose of each term using the diagram in Figures 2 and 9. It remains to verify this design and to quantify the relevance of each term. We also want to quantify the contribution of our novel VN+SC layer. For this purpose we

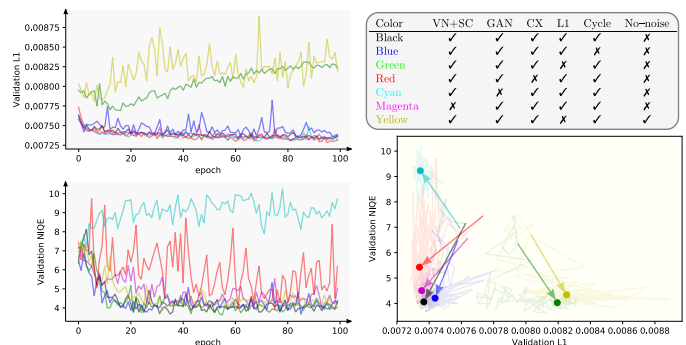


Fig. 15. Ablation tests show the validation scores when training our network for 100 epochs. We consider removal of the loss terms: GAN, CX, L1 and Cycle in (11), as well as VN+SC layers in the discriminator, and training the system without noise inputs.

trained MGBPv1 network architecture for 100 epochs using the loss function in section IV-B. In Figure 15 we show our measurements of L1 (distortion) and NIQE (perceptual) in a small validation set of 14 images after each epoch. We display the evolution through the number of epochs as well as the trajectories on the perception–distortion plane.

Overall, we see that our strategy adding all the losses (in black color) gives the best perception–distortion balance. In the extremes we see that removing the L1 and GAN losses

have catastrophic effects on distortion and perception, respectively. Still, these cases do not diverge to infinity because of other loss terms. Next, it is clear that the contextual loss helps improving the perceptual quality, and regarding distortion the amount of improvement is not conclusive. Then, the addition of the cycle loss shows a clear improvement over distortion, with inconclusive improvements on perceptual quality. And finally, we observe that the addition of the VN+SC layer in the discriminator clearly improves perceptual quality, although not as much as CX and GAN losses.

Figure 15 also shows a test in which we avoid the use of noise inputs by setting $W = 0$ in all losses. In this case we remove the L1 loss that would otherwise interfere with the GAN loss, causing a catastrophic effect. In this case distortion is controlled by the cycle loss, equivalent to how it is done in [55]. In this configuration the network performs slightly worse in perceptual quality and clearly worse on distortion, similar to only removing the L1 loss. In this case, we believe that the network uses the randomness in the input as innovation process, which cannot be controlled and limits the diversity.

C. Interpretability

Figure 16 shows interpretability results obtained by using the Deep Filter Visualization (DFV) method from [33]. To perform this complex analysis on a large model such as MGBPv2, with more than 20 million parameters, we use the so-called *Linescope* method recently introduced in [80]. For a given pixel in the input image (blue circles on the left side), Figure 16 displays the impulse response for the network model with frozen activations (all ReLU's acting as if the input image did not change). This represents the equivalent to an upscaling filter that adapts to the pixel location. In flat areas (example at the bottom of Figure 16) the upscaling filter looks isotropic and similar to a bicubic upscaler. In other locations, the filter strongly follows edges in hair and fingers, with receptive fields that extend for several hundred pixels. Overall, this confirms that the system has learned the geometry of the content.

VII. CONCLUSION

We have proposed the MultiGrid Back-Projection (MGBP) network architecture for image super-resolution. The network combines: first, a novel type of cross-scale residual block inspired in the IBP algorithm; and second, a multigrid recursion that uses cross-scale residual blocks within cross-scale residual blocks. The result is an architecture that balances computational complexity in an efficient and effective way, focusing more on lower resolutions and decreasing computations in higher resolutions. We also introduce a particular training strategy to achieve good perceptual quality by using noise inputs to traverse the perception-distortion plane. An interpretation using the concept of innovation jumps, together with ablation tests and results on international competitions prove the effectiveness of this strategy.

REFERENCES

[1] M. Sugawara, C. S-Y, and D. Wood, "Ultra-high-definition television (Rec. ITU-R BT.2020): A generational leap in the evolution of television," *Signal Processing Magazine, IEEE*, vol. 31, no. 3, pp. 170–174, May 2014. 1

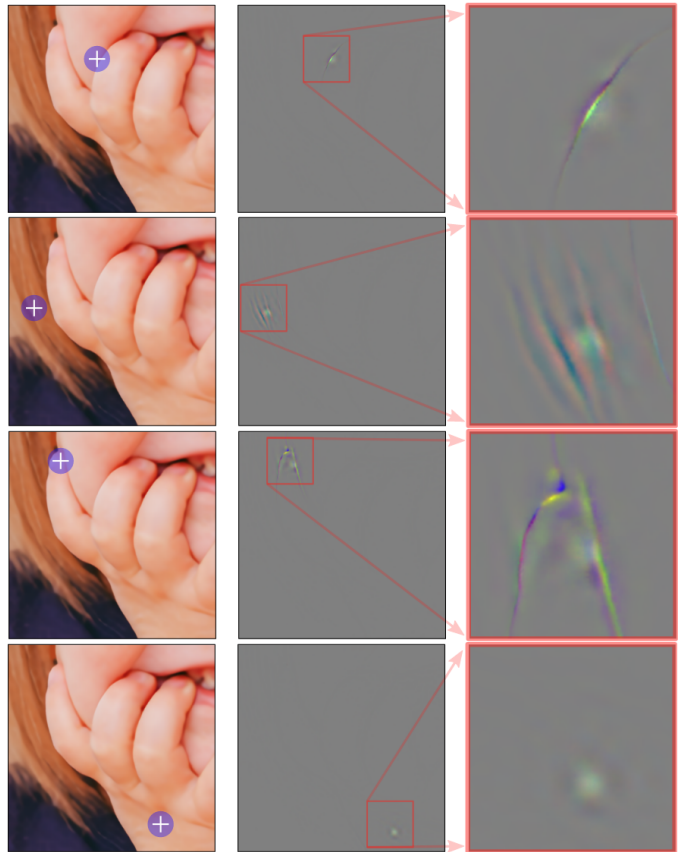


Fig. 16. Deep filter visualization (DFV) [33], [80] experiments on our MGBPv2 $16 \times$ model for the Fidelity track using a patch of size 767×767 . The model shows good knowledge of the geometry and large receptive fields.

- [2] J. Proakis and D. Manolakis, *Digital Signal Processing*, ser. Prentice Hall international editions. Pearson Prentice Hall, 2007. 1
- [3] S. Mallat, *A Wavelet Tour of Signal Processing*. Academic Press, 1998. 1
- [4] V. R. Algazi, G. E. Ford, and R. Potharlanka, "Directional interpolation of images based on visual properties and rank order filtering," in *Proc. IEEE Int. Conf. Acoustics, Speech, Signal Processing*, vol. 4. Toronto, ON: IEEE Signal Processing Society, May 1991, p. 3005–3008. 1
- [5] X. Li and M. T. Orchard, "New edge-directed interpolation," *IEEE Transactions on Image Processing*, vol. 10, no. 10, pp. 1521–1527, October 2001. 1
- [6] S. Mallat and G. Peyre, "A review of bandlet methods for geometrical image representation," *Numerical Algorithms*, vol. 44, no. 3, pp. 205–234, March 2007. 1
- [7] S. Park, M. Park, and M. Kang, "Super-resolution image reconstruction: a technical overview," *Signal Processing Magazine, IEEE*, vol. 20, no. 3, pp. 21–36, May 2003. 1
- [8] Y. LeCun, Y. Bengio, and G. Hinton, "Deep learning," *Nature*, vol. 521, no. 7553, pp. 436–444, May 2015. 1
- [9] C. Dong, C. C. Loy, K. He, and X. Tang, "Learning a deep convolutional network for image super-resolution," in *Proceedings of European Conference on Computer Vision (ECCV)*, 2014. 1, 9
- [10] K. He, X. Zhang, S. Ren, and J. Sun, "Deep residual learning for image recognition," *computer vision and pattern recognition*, pp. 770–778, 2016. 1, 5
- [11] B. Lim, S. Son, H. Kim, S. Nah, and K. M. Lee, "Enhanced deep residual networks for single image super-resolution," in *The IEEE Conference on Computer Vision and Pattern Recognition (CVPR) Workshops*, July 2017. 1, 5, 8, 9, 11
- [12] G. Huang, Z. Liu, L. van der Maaten, and K. Q. Weinberger, "Densely connected convolutional networks," in *Proceedings of the IEEE Conference on Computer Vision and Pattern Recognition*, 2017. 1, 8

- [13] Y. Zhang, Y. Tian, Y. Kong, B. Zhong, and Y. Fu, "Residual dense network for image super-resolution," in *CVPR*, 2018. 1
- [14] J. Hu, L. Shen, and G. Sun, "Squeeze-and-excitation networks," *computer vision and pattern recognition*, pp. 7132–7141, 2018. 1
- [15] Y. Zhang, K. Li, K. Li, L. Wang, B. Zhong, and Y. Fu, "Image super-resolution using very deep residual channel attention networks," in *Proceedings of the European Conference on Computer Vision (ECCV)*, 2018, pp. 286–301. 1, 9
- [16] X. Wang, R. B. Girshick, A. Gupta, and K. He, "Non-local neural networks," *computer vision and pattern recognition*, pp. 7794–7803, 2018. 1
- [17] Y. Zhang, K. Li, K. Li, B. Zhong, and Y. Fu, "Residual non-local attention networks for image restoration," *international conference on learning representations*, 2019. 1
- [18] S. Farsiu, M. Robinson, M. Elad, and P. Milanfar, "Fast and robust multiframe super resolution," *IEEE Transactions on Image Processing*, vol. 13, no. 10, pp. 1327–1344, 2004. 2
- [19] C. Liu and D. Sun, "On bayesian adaptive video super resolution," *IEEE Transactions on Pattern Analysis and Machine Intelligence*, vol. 36, no. 2, pp. 346–360, 2014. 2
- [20] Z. Ma, R. Liao, X. Tao, L. Xu, J. Jia, and E. Wu, "Handling motion blur in multi-frame super-resolution," in *2015 IEEE Conference on Computer Vision and Pattern Recognition (CVPR)*, 2015, pp. 5224–5232. 2
- [21] A. Kappeler, S. Yoo, Q. Dai, and A. K. Katsaggelos, "Video super-resolution with convolutional neural networks," *IEEE Transactions on Computational Imaging*, vol. 2, no. 2, pp. 109–122, 2016. 2
- [22] R. Liao, X. Tao, R. Li, Z. Ma, and J. Jia, "Video super-resolution via deep draft-ensemble learning," in *2015 IEEE International Conference on Computer Vision (ICCV)*, 2015, pp. 531–539. 2
- [23] D. Liu, Z. Wang, Y. Fan, X. Liu, Z. Wang, S. Chang, and T. Huang, "Robust video super-resolution with learned temporal dynamics," in *2017 IEEE International Conference on Computer Vision (ICCV)*, 2017, pp. 2526–2534. 2
- [24] X. Tao, H. Gao, R. Liao, J. Wang, and J. Jia, "Detail-revealing deep video super-resolution," in *2017 IEEE International Conference on Computer Vision (ICCV)*, 2017, pp. 4482–4490. 2
- [25] T. Xue, B. Chen, J. Wu, D. Wei, and W. T. Freeman, "Video enhancement with task-oriented flow," *International Journal of Computer Vision*, vol. 127, no. 8, pp. 1106–1125, 2019. 2, 10
- [26] Y. Jo, S. W. Oh, J. Kang, and S. J. Kim, "Deep video super-resolution network using dynamic upsampling filters without explicit motion compensation," in *2018 IEEE/CVF Conference on Computer Vision and Pattern Recognition*, 2018, pp. 3224–3232. 2, 10
- [27] X. Wang, K. C. Chan, K. Yu, C. Dong, and C. C. Loy, "Edvr: Video restoration with enhanced deformable convolutional networks," in *2019 IEEE/CVF Conference on Computer Vision and Pattern Recognition Workshops (CVPRW)*, 2019, pp. 0–0. 2, 10
- [28] J. Chen, X. Tan, C. Shan, S. Liu, and Z. Chen, "VESR-Net: The winning solution to youku video enhancement and super-resolution challenge," *arXiv preprint arXiv:2003.02115*, 2020. 2
- [29] Y. Zhang, K. Li, K. Li, L. Wang, B. Zhong, and Y. Fu, "Image super-resolution using very deep residual channel attention networks," in *Proceedings of the European Conference on Computer Vision (ECCV)*, 2018, pp. 294–310. 2, 10
- [30] D. Fuoli, Z. Huang, S. Gu, R. Timofte, A. Raventos, A. Esfandiari, S. Karout, X. Xu, X. Li, X. Xiong, J. Wang, P. Navarrete Michelini, W. Zhang, D. Zhang, H. Zhu, D. Xia, H. Chen, J. Gu, Z. Zhang, T. Zhao, S. Zhao, K. Akita, N. Ukita, H. P. S. D. Puthussery, and J. C. "AIM 2020 challenge on video extreme super-resolution: Methods and results," *arXiv preprint arXiv:2009.06290*, 2020. 2, 3, 8, 10
- [31] Y. Blau and T. Michaeli, "The perception-distortion tradeoff," in *The IEEE Conference on Computer Vision and Pattern Recognition (CVPR)*, June 2018. 2, 3, 11, 12
- [32] Y. Blau, R. Mechrez, R. Timofte, T. Michaeli, and L. Zelnik-Manor, "The 2018 pirm challenge on perceptual image super-resolution," in *Proceedings of the European Conference on Computer Vision (ECCV)*, 2018, pp. 0–0. 2, 3, 10, 11, 12, 13
- [33] P. Navarrete Michelini, H. Liu, and D. Zhu, "Multigrid backprojection super-resolution and deep filter visualization," in *Proceedings of the Thirty-Third AAAI Conference on Artificial Intelligence (AAAI 2019)*, AAAI, 2019. 2, 3, 4, 5, 6, 9, 14
- [34] —, "Multi-scale recursive and perception-distortion controllable image super-resolution," in *The European Conference on Computer Vision Workshops (ECCVW)*, September 2018. [Online]. Available: <http://arxiv.org/abs/1809.10711> 2, 8, 12
- [35] P. Navarrete Michelini, W. Chen, H. Liu, and D. Zhu, "MGBPV2: Scaling up multi-grid back-projection networks," in *The IEEE International Conference on Computer Vision Workshops (ICCVW)*, October 2019. [Online]. Available: <https://arxiv.org/abs/1909.12983> 2, 5, 6
- [36] U. Trottenberg and A. Schuller, *Multigrid*. Orlando, FL, USA: Academic Press, Inc., 2001. 2, 5, 6
- [37] R. Karras, T. Aila, S. Laine, and J. Lehtinen, "Progressive growing of GANs for improved quality, stability, and variation," in *International Conference on Learning Representations*, 2018. [Online]. Available: <https://openreview.net/forum?id=Hk99zCeAb> 3, 8
- [38] R. Timofte, S. Gu, J. Wu, L. Van Gool, L. Zhang, M.-H. Yang, and et al., "NTIRE 2018 challenge on single image super-resolution: Methods and results," in *The IEEE Conference on Computer Vision and Pattern Recognition (CVPR) Workshops*, June 2018. 3
- [39] M. Haris, G. Shakhnarovich, and N. Ukita, "Deep back-projection networks for super-resolution," in *IEEE Conference on Computer Vision and Pattern Recognition (CVPR)*, 2018. 3, 9
- [40] A. Lugmayr, M. Danelljan, R. Timofte, M. Fritsche, S. Gu, K. Purohit, P. Kandula, M. Suin, A. Rajagopalan, N. H. Joon et al., "AIM 2019 challenge on real-world image super-resolution: Methods and results," *arXiv preprint arXiv:1911.07783*, 2019. 3, 10, 12, 13
- [41] K. Seshadrinathan, R. Soundararajan, A. Bovik, and L. Cormack, "Study of subjective and objective quality assessment of video," *IEEE Transactions on Image Processing*, vol. 19, no. 6, pp. 1427–1441, June 2010. 3
- [42] Z. Wang, A. C. Bovik, H. R. Sheikh, and E. P. Simoncelli, "Image quality assessment: From error visibility to structural similarity," *IEEE TRANSACTIONS ON IMAGE PROCESSING*, vol. 13, no. 4, pp. 600–612, 2004. 3
- [43] H. R. Sheikh and A. C. Bovik, "Image information and visual quality," *Trans. Img. Proc.*, vol. 15, no. 2, pp. 430–444, Feb. 2006. [Online]. Available: <http://dx.doi.org/10.1109/TIP.2005.859378> 3
- [44] J. Johnson, A. Alahi, and F. Li, "Perceptual losses for real-time style transfer and super-resolution," *CoRR*, vol. abs/1603.08155, 2016. [Online]. Available: <http://arxiv.org/abs/1603.08155> 3
- [45] R. Mechrez, I. Talmi, and L. Zelnik-Manor, "The contextual loss for image transformation with non-aligned data," *arXiv preprint arXiv:1803.02077*, 2018. 3, 9, 11, 13
- [46] D. L. Ruderman, "The statistics of natural images," in *Network computation in neural systems*, vol. 5, no. 4, 1994, pp. 517–548. 3, 7, 8
- [47] A. Mittal, R. Soundararajan, and A. C. Bovik, "Making a "Completely Blind" Image Quality Analyzer," *IEEE Signal Processing Letters*, vol. 20, pp. 209–212, Mar. 2013. 3, 7, 9
- [48] A. Mittal, A. K. Moorthy, and A. C. Bovik, "No-reference image quality assessment in the spatial domain," *IEEE Trans. Image Process*, pp. 4695–4708, 2012. 3
- [49] R. Timofte, E. Agustsson, L. Van Gool, M.-H. Yang, L. Zhang et al., "NTIRE 2017 challenge on single image super-resolution: Methods and results," in *The IEEE Conference on Computer Vision and Pattern Recognition (CVPR) Workshops*, July 2017. 3
- [50] S. K. Mitter, "Nonlinear filtering of diffusion processes a guided tour," in *Advances in Filtering and Optimal Stochastic Control*, W. H. Fleming and L. G. Gorostiza, Eds. Berlin, Heidelberg: Springer Berlin Heidelberg, 1982, pp. 256–266. 3
- [51] M. Irani and S. Peleg, "Improving resolution by image registration," *CVGIP: Graph. Models Image Process.*, vol. 53, no. 3, pp. 231–239, Apr. 1991. [Online]. Available: [http://dx.doi.org/10.1016/1049-9652\(91\)90045-L](http://dx.doi.org/10.1016/1049-9652(91)90045-L) 4
- [52] T. H. Cormen, C. E. Leiserson, R. L. Rivest, and C. Stein, *Introduction to algorithms*. MIT press, 2009. 6
- [53] W.-S. Lai, J.-B. Huang, N. Ahuja, and M.-H. Yang, "Fast and accurate image super-resolution with deep laplacian pyramid networks," *arXiv:1710.01992*, 2017. 8, 9
- [54] A. Jolicœur-Martineau, "The relativistic discriminator: a key element missing from standard gan," *arXiv preprint arXiv:1807.00734*, 2018. 9
- [55] R. Mechrez, I. Talmi, F. Shama, and L. Zelnik-Manor, "Learning to maintain natural image statistics, [arxiv](https://arxiv.org/abs/1803.04626)," *arXiv preprint arXiv:1803.04626*, 2018. 9, 14
- [56] R. Timofte and V. D. Smet, "Gool, "A+": Adjusted anchored neighborhood regression for fast super-resolution," in *Proc. Asian Conf. Comput. Vis. (ACCV)*, 2014. 9
- [57] C. Dong, C. C. Loy, and X. Tang, "Accelerating the super-resolution convolutional neural network," in *Proceedings of European Conference on Computer Vision (ECCV)*, 2016. 9
- [58] J. Kim, J. K. Lee, and K. M. Lee, "Accurate image super-resolution using very deep convolutional networks," in *The IEEE Conference on Computer Vision and Pattern Recognition (CVPR Oral)*, June 2016. 9

- [59] W.-S. Lai, J.-B. Huang, N. Ahuja, and M.-H. Yang, "Deep laplacian pyramid networks for fast and accurate super-resolution," in *IEEE Conference on Computer Vision and Pattern Recognition*, 2017. 9
- [60] J. Kim, J. K. Lee, and K. M. Lee, "Deeply-recursive convolutional network for image super-resolution," in *The IEEE Conference on Computer Vision and Pattern Recognition (CVPR Oral)*, June 2016. 9
- [61] Y. Zhang, Y. Tian, Y. Kong, B. Zhong, and Y. Fu, "Residual dense network for image restoration," *IEEE Transactions on Pattern Analysis and Machine Intelligence*, 2020. 9
- [62] E. Agustsson and R. Timofte, "NTIRE 2017 challenge on single image super-resolution: Dataset and study," in *The IEEE Conference on Computer Vision and Pattern Recognition (CVPR) Workshops*, July 2017. 9
- [63] R. Zeyde, M. Elad, and M. Protter, "On single image scale-up using sparse-representations," in *International conference on curves and surfaces*. Springer, 2010, pp. 711–730. 9
- [64] D. Martin, C. Fowlkes, D. Tal, and J. Malik, "A database of human segmented natural images and its application to evaluating segmentation algorithms and measuring ecological statistics," in *Proceedings Eighth IEEE International Conference on Computer Vision. ICCV 2001*, vol. 2. IEEE, 2001, pp. 416–423. 9
- [65] J.-B. Huang, A. Singh, and N. Ahuja, "Single image super-resolution from transformed self-exemplars," in *Proceedings of the IEEE conference on computer vision and pattern recognition*, 2015, pp. 5197–5206. 9
- [66] Y. Matsui, K. Ito, Y. Aramaki, A. Fujimoto, T. Ogawa, T. Yamasaki, and K. Aizawa, "Sketch-based manga retrieval using manga109 dataset," *Multimedia Tools and Applications*, vol. 76, no. 20, pp. 21 811–21 838, 2017. 9
- [67] Y. Zhang, Y. Tian, Y. Kong, B. Zhong, and Y. Fu, "Evaluation code for residual dense networks," https://github.com/yulunzhang/RDN/blob/master/RDN_TestCode/Evaluate_PSNR_SSIM.m, 2018, [Online; accessed 20-May-2019]. 9
- [68] D. P. Kingma and J. Ba, "Adam: A method for stochastic optimization," *arXiv preprint arXiv:1412.6980*, 2014. 10
- [69] S. Nah, S. Baik, S. Hong, G. Moon, S. Son, R. Timofte, and K. M. Lee, "NTIRE 2019 challenge on video deblurring and super-resolution: Dataset and study," in *The IEEE Conference on Computer Vision and Pattern Recognition (CVPR) Workshops*, June 2019. 10
- [70] S. Kim, G. Li, D. Fuoli, M. Danelljan, Z. Huang, S. Gu, and R. Timofte, "The Vid3oC and IntVid datasets for video super resolution and quality mapping," in *2019 IEEE/CVF International Conference on Computer Vision Workshop (ICCVW)*. IEEE, 2019, pp. 3609–3616. 10
- [71] M. S. M. Sajjadi, B. Scholkopf, and M. Hirsch, "Enhancenet: Single image super-resolution through automated texture synthesis," in *The IEEE International Conference on Computer Vision (ICCV)*, Oct 2017. 11
- [72] S. Vasu, N. Thekke Madam, and A. Rajagopalan, "Analyzing perception-distortion tradeoff using enhanced perceptual super-resolution network," in *Proceedings of the European Conference on Computer Vision (ECCV)*, 2018. 12
- [73] M. Haris, G. Shakhnarovich, and N. Ukita, "Deep back-projection networks for single image super-resolution," *arXiv preprint arXiv:1904.05677*, 2019. 12
- [74] X. Wang, K. Yu, S. Wu, J. Gu, Y. Liu, C. Dong, Y. Qiao, and C. Change Loy, "Esrgan: Enhanced super-resolution generative adversarial networks," in *Proceedings of the European Conference on Computer Vision (ECCV)*, 2018, pp. 0–0. 12
- [75] M. Cheon, J.-H. Kim, J.-H. Choi, and J.-S. Lee, "Generative adversarial network-based image super-resolution using perceptual content losses," in *Proceedings of the European Conference on Computer Vision (ECCV)*, 2018. 12
- [76] J.-H. Choi, J.-H. Kim, M. Cheon, and J.-S. Lee, "Deep learning-based image super-resolution considering quantitative and perceptual quality," *arXiv preprint arXiv:1809.04789*, 2018. 12
- [77] T. Vu, T. M. Luu, and C. D. Yoo, "Perception-enhanced image super-resolution via relativistic generative adversarial networks," in *Proceedings of the European Conference on Computer Vision (ECCV)*, 2018. 12
- [78] X. Luo, R. Chen, Y. Xie, Y. Qu, and C. Li, "Bi-gans-st for perceptual image super-resolution," in *Proceedings of the European Conference on Computer Vision (ECCV)*, 2018. 12
- [79] K. Purohit, S. Mandal, and A. Rajagopalan, "Scale-recurrent multi-residual dense network for image super-resolution," in *Proceedings of the European Conference on Computer Vision (ECCV)*, 2018. 12
- [80] P. Navarrete Michelini, H. Liu, Y. Lu, and X. Jiang, "A tour of convolutional networks guided by linear interpreters," in *The IEEE*

International Conference on Computer Vision (ICCV). IEEE, Oct 2019. [Online]. Available: <https://arxiv.org/abs/1908.05168> 14

Pablo Navarrete Michelini was born in Santiago, Chile. He received the B.Sc. in Physics (2001), B.Sc. in Electrical Engineering (2001) and the Electrical Engineer Degree (2002), from Universidad de Chile at Santiago. He received the Ph.D. degree in Electrical Engineering from Purdue University at West Lafayette, in 2008. He worked as a research intern in CIMNE at Technical University of Catalonia in 2006, and as a visitor student research collaborator at Princeton University at Princeton, NJ, in 2006–2007. He was Assistant Professor in the Department of Electrical Engineering at Universidad de Chile in 2008–2011. He worked on video processing and compression at Yuvad Technologies in 2011–2013. He joined BOE Technology Group Co., Ltd in 2014 and he is currently a Research Scientist working on machine learning methods for image and video processing applications.

Wenbin Chen was born in Kaifeng, China. He received a Bachelor degree in Computer Science and Technology from Xidian University, in 2016, and a Master degree in Information Technology from Melbourne University, in 2019. He majored in Embedded System at bachelor level and then transferred to Artificial Intelligence for his master degree. He joined BOE Technology Group Co., Ltd in 2019 and he works on image and video processing applications.

Hanwen Liu was born in Shandong province, China. He received the Bachelor degree in Automation (2010) from Central South University at Changsha, Hunan province. He received the Master degree and Ph.D. (2016) in Armament Science and Technology from Beijing Institute of Technology at Beijing. He joined BOE Technology Group Co., Ltd after graduated in 2016 and he is currently a senior researcher working on deep learning methods for image processing applications.

Dan Zhu received the B.E. in Communications Engineering (2014) and M.E. in Communications Engineering (2017) from JiLin University in China. She joined BOE Technology Group Co., Ltd in 2017 and is currently working on deep learning methods for image and video processing applications.

Xingqun Jiang received his Ph.D. degree in Electrical and Computer Engineering at Cornell University in 2009, specialized in chip technology and computer graphics. In the past 10 years, Dr. Jiang has been working in the field of IOT and artificial intelligence constantly. He joined BOE Technology Group Co., Ltd in 2015, and now serves as Chief Technology Officer in the smart system business group, primarily responsible for the product and technology innovation. In recent years, Dr. Jiang has led his team to achieve significant progress in the research and development of artificial intelligence. In 2019, they won three global championships in image super-resolution, object detection and gesture recognition, respectively. More than 20 products and solutions powered by artificial intelligence technology has been made and delivered to customers in different markets. Dr. Jiang's team has totally contributed over 2200 patents to the corporate, making BOE ranked as 6th in terms of AI patents among all the Chinese corporates.

Currently, Dr. Jiang and his team is focused on intelligent graphics and computer vision, continuing the product and technology innovation in IOT and artificial intelligence.